Available online at www.sciencedirect.com

ScienceDirect

Journal of Solid State Chemistry 179 (2006) 3420–3428

JOURNAL OF SOLID STATE CHEMISTRY

www.elsevier.com/locate/jssc

Crystal structure and phase transformations of calcium yttrium orthophosphate, $Ca_3Y(PO_4)_3$

Koichiro Fukuda*, Tomoyuki Iwata, Takahiro Niwa

Department of Environmental and Materials Engineering, Nagoya Institute of Technology, Nagoya 466-8555, Japan

Received 28 April 2006; received in revised form 20 June 2006; accepted 3 July 2006

Abstract

Crystal structure and phase transformations of calcium yttrium orthophosphate $Ca_3Y(PO_4)_3$ were investigated by X-ray powder diffraction, selected-area electron diffraction, transmission electron microscopy and optical microscopy. The high-temperature phase is isostructural with eulytite, cubic (space group $I\bar{4}3d$) with $a = 0.983320(5)\,\mathrm{nm}$, $V = 0.950790(8)\,\mathrm{nm}^3$, $Z = 4$ and $D_x = 3.45\,\mathrm{Mg\,m}^{-3}$. The crystal structure was refined with a split-atom model, in which the oxygen atoms are distributed over two partially occupied sites. Below the stable temperature range of eulytite, the crystal underwent a martensitic transformation, which is accompanied by the formation of platelike surface reliefs. The inverted crystal is triclinic (space group $P1$) with $a = 1.5726(1)\,\mathrm{nm}$, $b = 0.84267(9)\,\mathrm{nm}$, $c = 0.81244(8)\,\mathrm{nm}$, $\alpha = 109.739(4)^\circ$, $\beta = 90.119(5)^\circ$, $\gamma = 89.908(7)^\circ$, $V = 1.0134(1)\,\mathrm{nm}^3$, $Z = 4$ and $D_x = 3.24\,\mathrm{Mg\,m}^{-3}$. The crystal grains were composed of pseudo-merohedral twins. The adjacent twin domains were related by the pseudo-symmetry mirror planes parallel to $\{10\bar{1}\}$ with the composition surface $\{10\bar{1}\}$. When the eulytite was cooled relatively slowly from the stable temperature range, the decomposition reaction of $Ca_3Y(PO_4)_3 \rightarrow \beta\text{-}Ca_3(PO_4)_2 + YPO_4$ occurred.

Keywords: Calcium yttrium orthophosphate; High temperature XRD; Rietveld method; Martensitic transformation; Eulytite-type structure

1. Introduction

The $Ca_3(PO_4)_2$–YPO_4 binary system contains one intermediate compound $Ca_3Y(PO_4)_3$, which is stable over the temperature range 2063–1488 K, while it decomposes into β-$Ca_3(PO_4)_2$ and YPO_4 below 1488 K [1,2]. The compound is quenchable to ambient temperature, and its X-ray powder diffraction (XRPD) pattern is very similar to that of eulytite, $Bi_4(SiO_4)_3$ [3–5]. Eulytite is cubic with space group $I\bar{4}3d$. In the crystal structure, bismuth is located on 16*c* position, silicon on 12*a*, and oxygen on 48*e*. The combined substitutions of Si^{4+} by P^{5+} and Bi^{3+} by appropriate cations necessary for charge compensation yield the eulytite-type phosphates with the formulae $A_3B(PO_4)_3$ and $A_7C(PO_4)_6$, where A = divalent cation (e.g., Ca, Sr and Ba), B = trivalent cation (e.g., rare earths) and C = tetravalent cation (e.g., Sn, Hf and Zr) [6]. However, in spite of the abundance of these phosphates, the structural analyses by X-ray and/or neutron diffraction have been carried out only for the compounds $Ca_3Bi(PO_4)_3$ [7], $Ba_3La(PO_4)_3$ [7], $Ba_3Bi(PO_4)_3$ [6] and $Sr_3La(PO_4)_3$ [5]. All of these compounds showed the positional disorder of oxygen atoms, which were distributed over two or three partially occupied sites. The compound $Ba_3Bi(PO_4)_3$ contained, contrary to the other compounds, two distinguished sites for Ba^{2+} and Bi^{3+}.

One of the characteristics necessary and sufficient for martensitic transformations is displaciveness involving a shape deformation [8]. Thus, reliefs are formed on prepolished surface of the parent-phase crystal; the resultant martensite regions observed by optical microscopy are generally plate shaped. According to the observed kinetics, the martensitic transformations can be divided into two distinct classes; athermal and isothermal martensite. In athermal martensite, the transformation progresses with decreasing temperature, whereas in isothermal martensite, the fraction transformed increases with

---

*Corresponding author. Fax: +81 52 735 5289.

E-mail address: fukuda.koichiro@nitech.ac.jp (K. Fukuda).

0022-4596/$ - see front matter © 2006 Elsevier Inc. All rights reserved.
doi:10.1016/j.jssc.2006.07.013

time at a constant temperature. This implies that the progress of the latter transformation can be inhibited by rapid cooling.

Intracrystalline microtextures (e.g., twinning) are often induced by phase transformations, which involve changes in the space group symmetry [9]. The loss of a point symmetry element during the transformation results in the formation of twin domains. If the high- and low-symmetry phases are of the same crystal system, the twinning is by merohedry. On the other hand, the change in crystal system results in the formation of pseudo-merohedral twins. Since the lattices of such twins are not exactly coincident, the adjacent twins produce slightly split diffraction spots.

In the present study, we have revealed the structural disorder of eulytite-type $Ca_3Y(PO_4)_3$. Below the stable temperature range of eulytite, the martensitic transformation occurred. The resulting crystal was examined by XRPD as well as electron diffraction to derive the crystallographic data.

2. Experimental

2.1. Sample preparation

The present specimen of $Ca_3Y(PO_4)_3$ was prepared from stoichiometric amounts of reagent-grade chemicals $CaCO_3$, Y_2O_3 and $NH_4H_2PO_4$. The mixture was pressed into pellets (12 mm diameter and 3 mm thick), heated at 1623 K for 24 h, followed by quenching in water and/or in air. The cooling rates of the quenched specimen (termed S-Q) were estimated to be higher than 200 K/s in the temperature range ~1400–1000 K.

Parts of the samples S-Q were reheated at 1623 K for 1 h, cooled at seven different rates (i.e., ~7, ~1, ~0.7 K/s, 20, 5, 3.3 and 1.7 K/min) to ~500 K, then quenched in air. The samples thus obtained were termed S-(7 K/s), S-(1 K/s), S-(0.7 K/s), S-(20 K/min), S-(5 K/min), S-(3.3 K/min) and S-(1.7 K/min) with decreasing cooling rate. The cooling rate of ~0.7 K/s was achieved by cutting furnace power. The cooling rates higher than 0.7 K/s were realized by blowing air into the furnace. With cooling slower than 0.7 K/s, the furnace temperature was linearly decreased under controlled conditions.

2.2. Characterization

With eulytite-type $Ca_3Y(PO_4)_3$, X-ray powder diffraction (XRPD) intensities for structural refinement were collected on a PANalytical X'Pert PRO Alpha-1 diffractometer equipped with a high speed detector (X'Celerator) in Bragg–Brentano geometry using monochromatized $CuK\alpha_1$ radiation (45 kV, 40 mA). Other experimental conditions were: continuous scan, 2θ range from 20.0042° to 148.9567° with the total number of 15434 datapoints. The crystal-structure models were visualized with a software package VENUS [10]. The XRPD patterns for phase identification and for determination of unit-cell dimensions and integrated intensities were collected on a PANalytical X'Pert diffractometer in Bragg–Brentano geometry using $CuK\alpha$ radiation (50 kV, 40 mA) and a step-scan technique in a 2θ range from 10° to 60° ($\Delta 2\theta = 0.02°$) with a fixed counting time (t) of 15 s/step. A programmable divergence slit was employed to maintain an illumination length of 10 mm on the sample.

Structural changes at high temperatures were examined by the latter diffractometer equipped with a heating stage. The profile intensity data during stepwise heating up to 1473 K (step width = ~100 K) were collected in a 2θ range from 20° to 50° with $t = 2$ s/step. Powder specimens were deposited with ethyl alcohol on the platinum heating filament ($132 \times 9 \times 1$ mm). The programmable divergence slit was employed to maintain an illumination area of 10×9 mm regardless of the 2θ value. The thermal behavior was also investigated by a differential thermal analysis (DTA, Model TG8120, Rigaku Co., Tokyo, Japan) up to 1473 K. The temperature was controlled by a Pt–PtRh (10%) thermocouple, with heating rate of 10 K/min.

Several quenched pellets of S-Q were polished with diamond paste to form a flat surface, followed by reheating at 773 K for 1 h. The resulting reliefs on the prepolished surface were observed using a differential interference microscope.

The samples were examined by a transmission electron microscope (JEM 2010) operated at 200 kV and equipped with a double-tilting stage. The crystal fragments were crushed using an agate mortar and deposited with ethyl alcohol on a copper grid. Selected area electron diffraction (SAED) patterns and corresponding lattice images were obtained.

3. Results and discussion

3.1. Disordered structure of eulytite-type $Ca_3Y(PO_4)_3$

The sample S-Q was exclusively composed of the eulytite-type $Ca_3Y(PO_4)_3$ crystals. The peak positions of the XRPD pattern were determined on a computer program POWDERX [11], followed by the indexing procedure on a computer program TREOR90 [12]. In the latter procedure, 2θ values of 20 peak positions were used as input data. Only one cubic cell was found with satisfactory figures of merit $M_{20}/F_{20} = 92/47(0.003811,114)$ [13,14]. The SAED patterns in Fig. 1 can be well accounted for by the derived unit-cell dimension of $a = 0.98314(1)$ nm. Because the relative intensities of individual reflections of the XRPD pattern were very similar to those of the eulytite-type compounds, the atomic positions of the initial structural model were identical to those of $Bi_4(SiO_4)_3$ [5]. The structural parameters were refined by the Rietveld method on a computer program RIETAN-2000 [15]. The background intensities were fitted to a polynomial function with 12 adjustable parameters. The split pseudo-Voigt function

[16] was used to fit the peak profile. Isotropic atomic displacement parameters, B, were assigned to all atoms.

The B parameter of oxygen atom showed particularly large value of 0.136(1) nm^2, with less satisfactory reliability indices [17] of $R_{\mathrm{wp}} = 8.76\%$, $R_{\mathrm{p}} = 6.91\%$, $R_{\mathrm{B}} = 8.13\%$ and $S = 1.75$. Ionic radii of P^{5+} in the four-fold coordination $[r(\mathrm{P}^{5+}) = 0.017\,\mathrm{nm}$ and $r(\mathrm{O}^{2-}) = 0.138\,\mathrm{nm}]$ predict the interatomic distance of 0.155 nm for P–O [18]. However, the P–O bond length is 0.1481(3) nm, being appreciably shorter than the expected value. Accordingly, the present initial model was, in the subsequent refinement process, modified to a split-atom model, the oxygen atoms in which are distributed over two partially occupied sites. The individual occupancies were finally refined under the

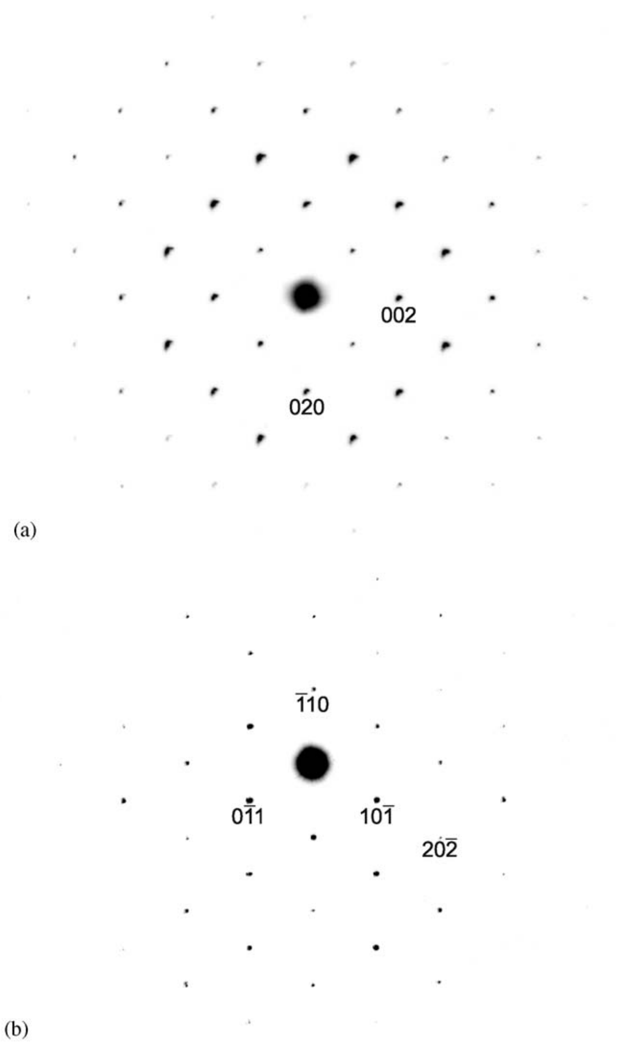

Fig. 1. Selected-area electron diffraction patterns of eulytite-type $\mathrm{Ca_3Y(PO_4)_3}$. Incident beam nearly parallel to (a) [100] and (b) [111].

Table 1
Crystal data of eulytite-type calcium yttrium orthophosphate

Chemical composition	$\mathrm{Ca_3Y(PO_4)_3}$
Space group	$I\bar{4}3d$
a (nm)	0.983320(5)
V (nm^3)	0.950790(8)
Z	4
D_x ($\mathrm{Mg\,m^{-3}}$)	3.45

Table 2
Structural parameters of eulytite-type calcium yttrium orthophosphate

Atom	g	Site	x	y	z	$100 \times B/\mathrm{nm}^2$
M^{a}	1.0	16c	0.06773(5)	x	x	3.21(2)
P	1.0	12a	0.375	0	0.25	2.85(3)
O1	0.538(4)	48e	0.0059(4)	0.1137(4)	0.2976(4)	6.79(9)
O2	0.462	48e	0.0943(5)	0.1550(5)	0.2880(4)	6.79

[a] $M = 0.75\mathrm{Ca} + 0.25\mathrm{Y}$.

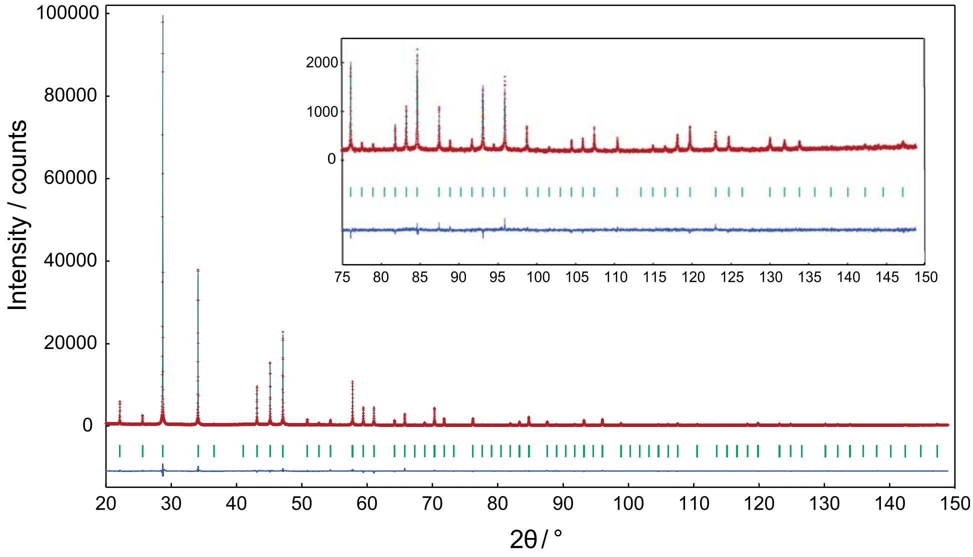

Fig. 2. Comparison of observed diffraction pattern of the eulytite-type calcium yttrium orthophosphate (symbol: +) with the corresponding calculated pattern (upper solid line) by the Rietveld refinement. The difference curve is shown in the lower part of the diagram. Vertical bars indicate the positions of Bragg reflections.

constraint that the total number of oxygen atoms on these sites was unchanged.

In the split-atom model, the reliability indices ($R_{\mathrm{wp}} = 7.11\%$, $R_{\mathrm{p}} = 5.34\%$, $R_{\mathrm{B}} = 4.06\%$ and $S = 1.42$) as well as the B values of oxygen atoms (O1 and O2) significantly decreased as compared with those of the initial model (Fig. 2). The crystal data are given in Table 1, and the positional and B parameters of atoms are given in Table 2. The P–O1 and P–O2 bond lengths in the PO_4 tetrahedra (Table 3) are in good agreement with those expected from the ionic radius as well as bond valence sum (0.152 nm). The M–O1 and M–O2 bond lengths (Table 3) range from, respectively, 0.230–0.326 and 0.235–0.273 nm. The mean M–O2 bond length of 0.2567 nm is in accord with the expected weighted bond distance of 0.257 nm [$r(\mathrm{Ca}^{2+}(9)) = 0.118$ nm, $r(\mathrm{Y}^{3+}(9)) = 0.1075$ nm and $r(\mathrm{O}^{2-}(8)) = 0.142$ nm] for $M = 0.75\mathrm{Ca} + 0.25\mathrm{Y}$ [18]. The resultant structural model is compatible with those of $Ca_3Bi(PO_4)_3$ and $Ba_3La(PO_4)_3$ (Fig. 3). We have also refined the other structural models with three positions for oxygen atoms and/or two distinguished sites for Ca^{2+} and Y^{3+}. However, the reliability indices of these models did not decrease significantly as compared with those of the former split-atom model.

Table 3
Selected bond lengths (nm) and angles (deg) in eulytite-type calcium yttrium orthophosphate

M–O1	0.2303(3) × 3
	0.2384(4) × 3
	0.3259(4) × 3
〈M–O1〉	0.2649
M–O2	0.2345(4) × 3
	0.2622(4) × 3
	0.2734(6) × 3
〈M–O2〉	0.2567
P–O1	0.1543(4) × 4
P–O2	0.1570(4) × 4
O1–P–O1	104.1(1) × 4
	120.9(3) × 2
〈O1–P–O1〉	109.7
O2–P–O2	107.3(1) × 4
	114.0(2) × 2
〈O2–P–O2〉	109.5

3.2. Martensitic transformation

When the crystals of eulytite in sample S-Q were reheated at 773 K for 1 h, platelike reliefs appeared on the prepolished surface (Fig. 4). These plates must have been formed by a martensitic transformation, because the shape deformation is one of the most important characteristic of the transformation. The probable unit-cell

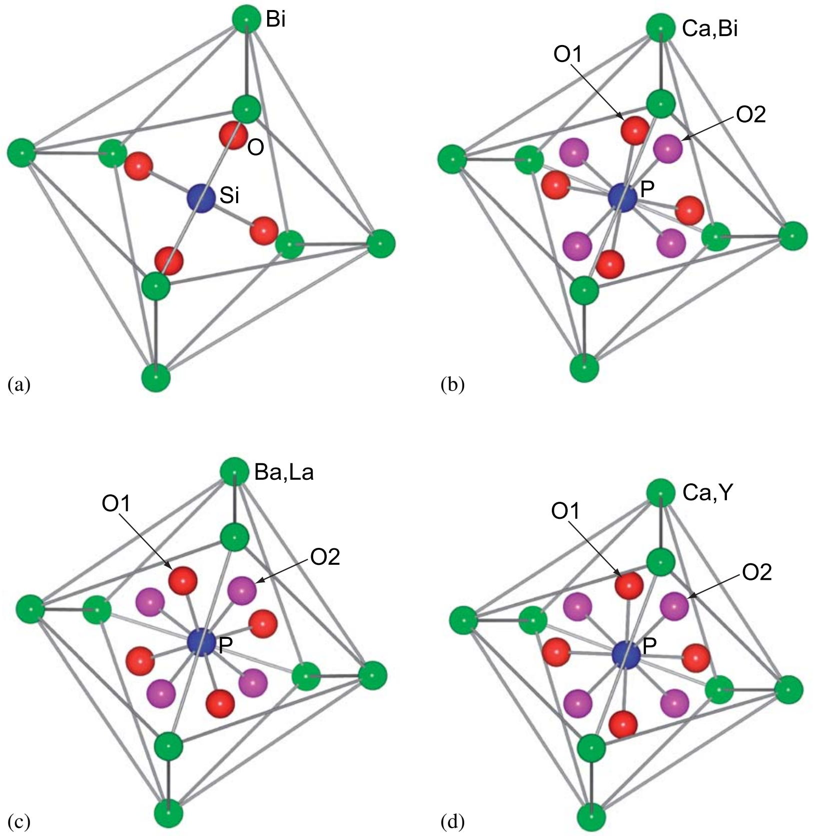

(a) (b) (c) (d)

Fig. 3. Part of the structure viewed along the [001] direction for (a) $Bi_4(SiO_4)_3$ [5], (b) $Ca_3Bi(PO_4)_3$ [7], (c) $Ba_3La(PO_4)_3$ [7] and (d) $Ca_3Y(PO_4)_3$.

parameters of the martensite phase (termed "inverted eulytite") were derived from the SAED patterns (Fig. 5); the cell dimensions were $a \approx 1.57$ nm, $b \approx 0.84$ nm, $c \approx 0.81$ nm, $\alpha \approx 110°$, $\beta \approx 90°$ and $\gamma \approx 90°$. The cell dimensions as well as integrated intensities were refined by the whole powder-pattern decomposition method in the 2θ range from 10° to 30°, based on the Pawley algorithm [19], on a computer program WPPF (the final reliability indices $R_{wp} = 5.08\%$ and $R_p = 3.57\%$) [20]. The refined cell parameters in triclinic system (Table 4) could index all reflections in the observed XRPD pattern (Fig. 6). Because the symmetry of the parent eulytite is noncentrosymmetric (space group $I\bar{4}3d$), the space group of the inverted eulytite would be $P1$ (noncentrosymmetric). The integrated intensity parameters (I) and their estimated standard deviations [$\sigma(I)$] are given in Table 5. For the closely overlapping reflections, the individual intensities were equipartitioned.

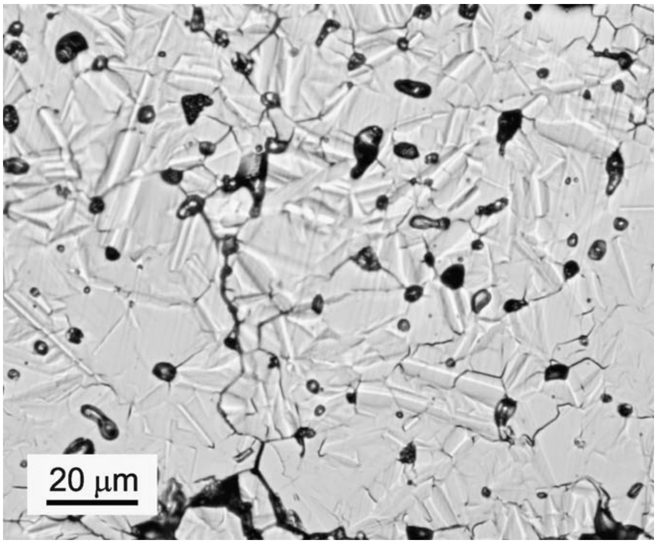

Fig. 4. Platelike surface reliefs associated with the martensitic transformation on heating at 773 K for 1 h. Differential interference microscopy.

Table 4
Crystal data of inverted calcium yttrium orthophosphate

Chemical composition	$Ca_3Y(PO_4)_3$
Space group	$P1$
a (nm)	1.5726(1)
b (nm)	0.84267(9)
c (nm)	0.81244(8)
α (deg)	109.739(4)
β (deg)	90.119(5)
γ (deg)	89.908(7)
V (nm^3)	1.0134(1)
Z	4
D_x (Mg m^{-3})	3.24

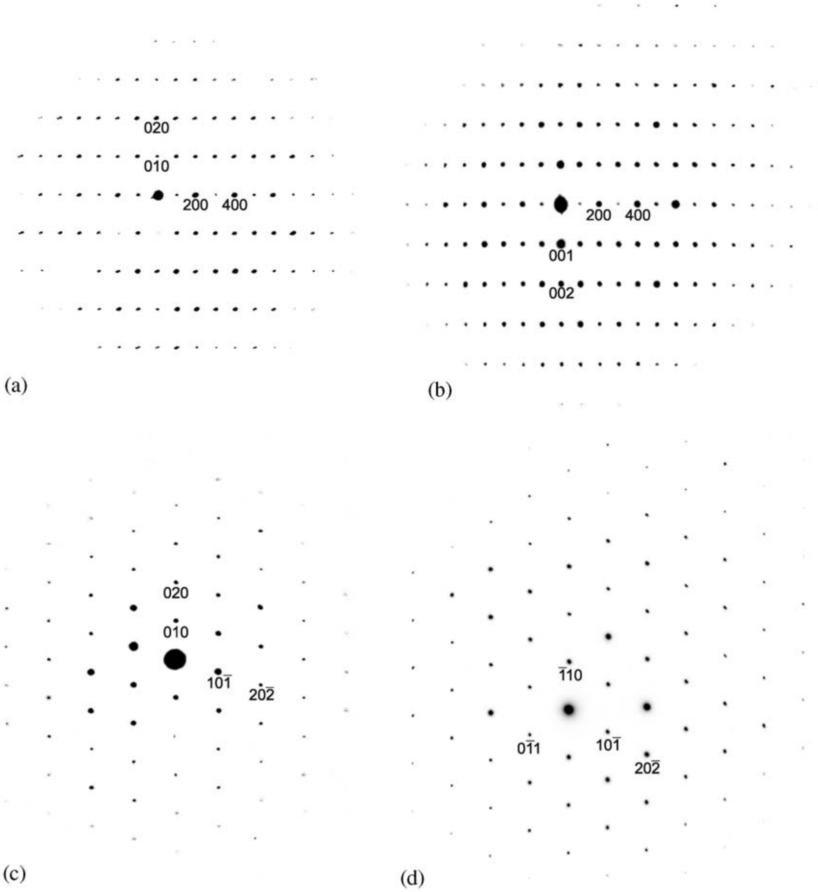

Fig. 5. Selected-area electron diffraction patterns of inverted $Ca_3Y(PO_4)_3$. Incident beam nearly parallel to (a) [001], (b) [010], (c) [101] and (d) [111].

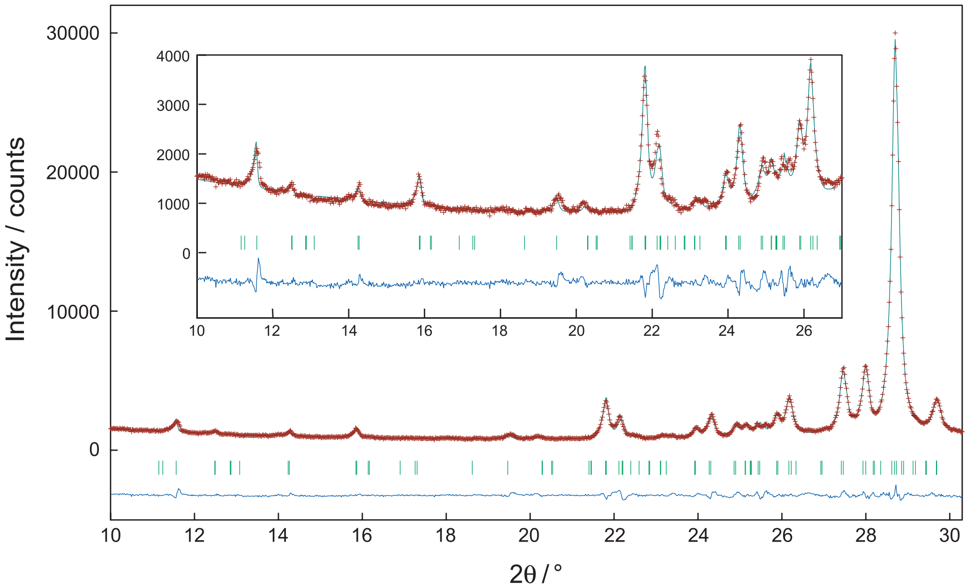

Fig. 6. Comparison of observed diffraction pattern of the inverted calcium yttrium orthophosphate (symbol: +) with the corresponding calculated pattern (upper solid line) by the Pawley method. The difference curve is shown in the lower part of the diagram. Vertical bars indicate the positions of Bragg reflections.

Values of d-spacing (d_{calc}) and scattering angle ($2\theta_{\text{calc}}$) were determined from the unit-cell parameters. The XRPD patterns of S-(7 K/s) and S-(1 K/s) showed that these crystals were also composed exclusively of the inverted eulytite.

The SAED pattern in Fig. 7(a) shows spot splitting, which indicates that it is obtained from the two orientational domains related by pseudo-merohedral twinning. The microscopic observation along $\langle 010 \rangle$ confirms that the composition surface, which separates the two twin domains, denoted by I and II, is parallel to $\{10\bar{1}\}$ (Fig. 7(b)). The schematic diagram in Fig. 8 shows the exact lattice fit along the composition surface for the adjacent twin domains.

The SAED pattern of the inverted eulytite (I) in Fig. 5(d) shows a marked resemblance to that of the parent eulytite (E) in Fig. 1(b), both incident beams of which are parallel to $\langle 111 \rangle$. This implies that there must be a definite orientation relationship between the lattices of the parent and inverted eulytite. The pseudo-symmetry triad axes exist along $\langle 111 \rangle_{\mathrm{I}}$, which would originally be the triad axes along $\langle 111 \rangle_{\mathrm{E}}$. In addition, the diffraction spot with indices $1\,0\,\bar{1}_{\mathrm{I}}$ (Fig. 5(d)) corresponds to that of $1\,0\,\bar{1}_{\mathrm{E}}$ (Fig. 1(b)) in the reciprocal space, hence the $\{10\bar{1}\}_{\mathrm{I}}$ planes would be parallel to those of $\{10\bar{1}\}_{\mathrm{E}}$ in the real space. Accordingly, the orientation relationship between the parent and inverted eulytite would be expressed as follows:

$$\{10\bar{1}\}_{\mathrm{E}} // \{10\bar{1}\}_{\mathrm{I}} \text{ and } \langle 111 \rangle_{\mathrm{E}} // \langle 111 \rangle_{\mathrm{I}}.$$

Because the twinning is pseudo-merohedral, the point group symmetry elements of the former high-symmetry (eulytite) phase must have been lost during the transformation.

The orientation of twin boundaries induced by phase transformations is, in general, determined by the condition such that the low-symmetry phase tends to maintain the total symmetry of the high-symmetry phase as a statistical average. In the high-symmetry (eulytite) phase with point group $\bar{4}3m$, the mirror planes exist parallel to $\{10\bar{1}\}_{\mathrm{E}}$, which correspond to $\{10\bar{1}\}_{\mathrm{I}}$ of the low-symmetry (inverted) phase. Accordingly, the adjacent twin domains I and II in Figs. 7(b) and 8 are most probably related by the pseudo-symmetry mirror planes parallel to $\{10\bar{1}\}$.

The symmetry elements that are confirmed to be lost during the high–low transformation are triad axes along $\langle 111 \rangle_{\mathrm{E}}$ and mirror planes parallel to $\{10\bar{1}\}_{\mathrm{E}}$. When these symmetry elements were lost from the point group $\bar{4}\,3\,m$, the resulting point group is $2\,2\,2$ (the loss of mirror planes results in the point group 23, and the subsequent loss of triad axes leads to the point group $2\,2\,2$). If one of the three diad axes (along $\langle 100 \rangle_{\mathrm{E}}$) corresponded to the a-axis of the inverted eulytite (along $[100]_{\mathrm{I}}$), the crystal could be monoclinic with $\beta = \gamma = 90^\circ$. However, the crystallographic orientation relationship indicates that these two directions make an angle of $\approx 19^\circ$ ($= [100]_{\mathrm{E}} \hat{} [100]_{\mathrm{I}}$) and hence the inverted eulytite is most probably triclinic.

3.3. Reactions occurring on cooling

When the samples of S-Q were cooled at ~0.7 K/s and 20 K/min, the decomposition reaction of $Ca_3Y(PO_4)_3 \rightarrow \beta\text{-}Ca_3(PO_4)_2 + YPO_4$ occurred, but the process was not completed because the obtained samples S-(0.7 K/s) and S-(20 K/min) were composed of the three phases. On the other hand, the samples S-(5 K/min), S-(3.3 K/min) and S-(1.7 K/min) were exclusively made up of the $\beta\text{-}Ca_3(PO_4)_2$

Table 5
Powder data of inverted calcium yttrium orthophosphate

h	k	1	$2\theta_{calc}$ (deg)	d_{calc} (nm)	I	$\sigma(I)$	I/I_o
0	1	0	11.15	0.7777	2.3	8.4	1
2	0	0	11.24	0.7710	1.6	8.4	1
0	0	1	11.56	0.7498	165.1	8.7	55
1	1	0	12.48	0.6947	17.2	3.7	6
−1	1	0	12.49	0.6941	17.2		6
−1	−1	1	14.23	0.6097	26.9	3.6	9
1	−1	1	14.26	0.6087	26.9		9
2	1	0	15.85	0.5478	64.7	3.9	22
−2	1	0	15.87	0.5473	64.7		22
−2	0	1	16.14	0.5379	4.6	3.3	2
2	0	1	16.17	0.5371	4.6		2
−1	1	1	19.47	0.4468	40.9	3.7	14
1	1	1	19.47	0.4467	40.9		14
3	1	0	20.28	0.4290	22.9	3.6	8
−3	1	0	20.30	0.4286	22.9		8
−2	1	1	21.80	0.3993	366.1	6.6	122
2	1	1	21.81	0.3992	366.1		122
0	−1	2	22.12	0.3937	130.9	3.9	44
−1	−2	1	22.19	0.3925	130.9		44
1	−2	1	22.21	0.3922	130.9		44
0	2	0	22.40	0.3889	14.1	9.0	5
4	0	0	22.60	0.3855	40.8	8.2	14
1	2	0	23.11	0.3771	15.2	4.8	5
−1	2	0	23.12	0.3770	15.2		5
0	0	2	23.25	0.3749	59.6	9.4	20
−1	0	2	23.92	0.3644	85.6	4.9	29
1	0	2	23.94	0.3642	85.6		29
−2	−2	1	24.27	0.3593	227.7	6.0	76
2	−2	1	24.31	0.3587	227.7		76
−2	−1	2	24.86	0.3509	82.2	5.6	27
2	−1	2	24.90	0.3503	82.2		27
2	2	0	25.12	0.3473	106.0	8.5	35
−2	2	0	25.14	0.3471	106.0		35
−3	1	1	25.25	0.3456	14.8	4.0	5
4	1	0	25.25	0.3455	14.8		5
3	1	1	25.26	0.3455	14.8		5
−4	1	0	25.27	0.3453	14.8		5
−4	0	1	25.44	0.3431	92.5	6.0	31
4	0	1	25.47	0.3426	92.5		31
−2	0	2	25.87	0.3374	193.2	6.6	65
2	0	2	25.91	0.3369	193.2		65
−4	−1	1	26.17	0.3336	382.5	10.5	128
4	−1	1	26.22	0.3329	382.5		128
0	−2	2	26.33	0.3316	58.8	16.1	20
−1	−2	2	26.93	0.3243	21.1	5.7	7
1	−2	2	26.96	0.3240	21.1		7
−3	−2	1	27.41	0.3188	665.6	11.4	222
3	−2	1	27.47	0.3182	665.6		222
−3	−1	2	27.94	0.3129	698.5	13.8	233
3	−1	2	28.00	0.3122	698.5		233
0	2	1	28.62	0.3056	2995.3	38.7	1000
−2	−2	2	28.69	0.3049	2995.3		1000
2	−2	2	28.74	0.3044	2995.3		1000
0	1	2	29.13	0.3004	8.5	6.6	3
1	2	1	29.19	0.2998	8.5		3
−1	2	1	29.19	0.2998	8.5		3
−4	1	1	29.44	0.2973	7.4	7.3	2
4	1	1	29.45	0.2972	7.4		2
−1	1	2	29.68	0.2949	363.3	9.3	121
1	1	2	29.69	0.2948	363.3		121

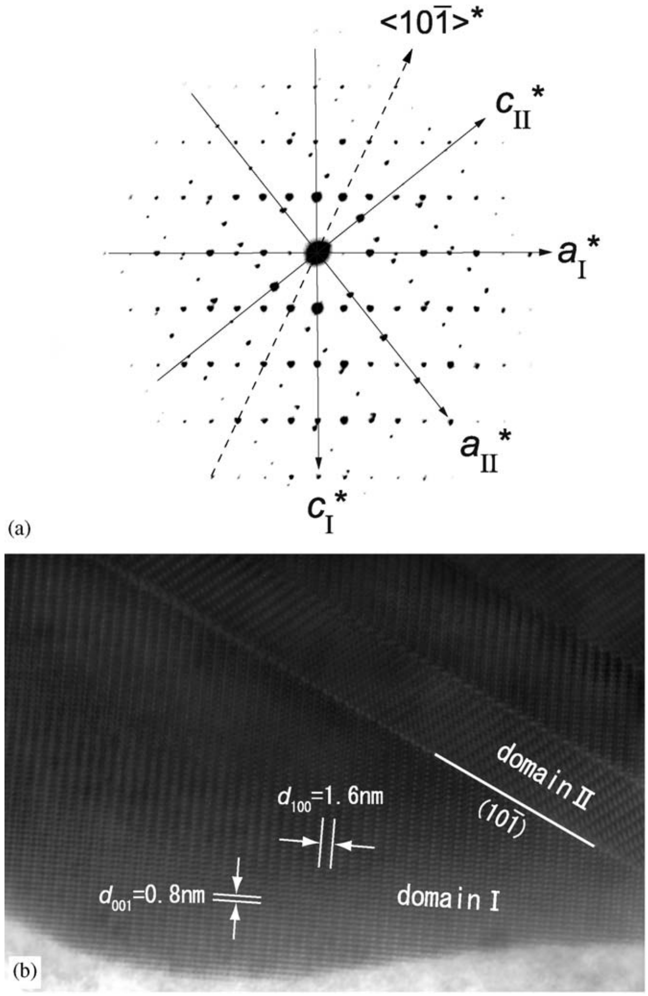

Fig. 7. (a) Selected area electron diffraction pattern showing pseudo-merohedral twinning and (b) corresponding lattice image. Incident beam nearly parallel to [010]. The two twin domains I and II have the common zone axes $\langle 101 \rangle$ and $\langle 010 \rangle$, and therefore, have a common plane $\{10\bar{1}\}$.

and YPO_4 crystals, indicating that the decomposition reaction was completed after cooling at rates lower than ~5 K/min.

The high-temperature XRPD patterns showed that, during heating, the eulytite was stable up to 473 K (Fig. 9). On further heating, the XRPD pattern at 573 K was of the inverted eulytite, and it was nearly unchanged up to 1173 K. At 1273 K, the XRPD showed that the decomposition reaction of $Ca_3Y(PO_4)_3 \rightarrow Ca_3(PO_4)_2 + YPO_4$ started, and it was nearly completed at 1373 K (Fig. 9). The two endothermic effects of DTA at 523 K ($= T_m$) and 1182 K ($= T_d$) during heating are therefore assigned as the starting temperatures of the martensitic transformation and decomposition reaction, respectively.

During the heating and/or cooling processes of eulytite, the martensitic transformation and decomposition reaction occurred. In order to clearly account for the dependence of phase constitution on time and temperature,

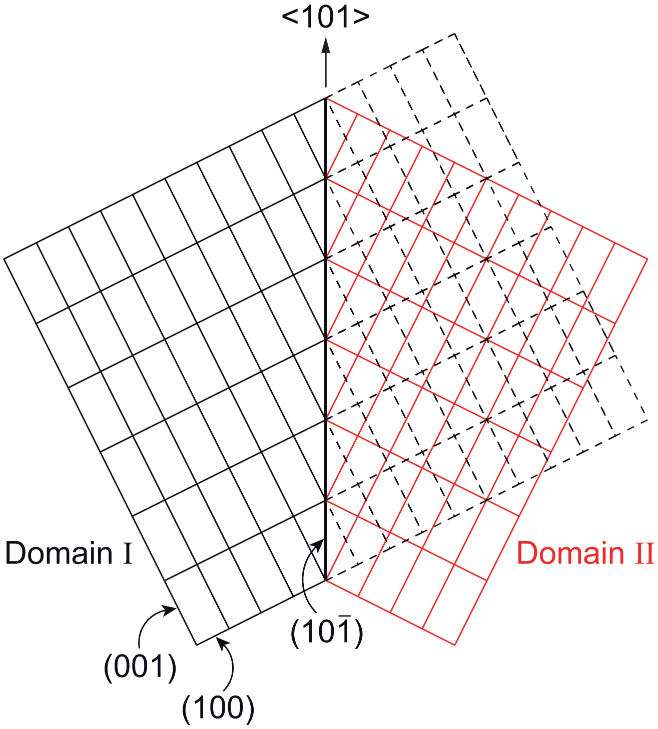

Fig. 8. Schematic diagram of the twin domains juxtaposed on composition surface $(10\bar{1})$, viewed along [010]. The pseudo-symmetry mirror plane is parallel to the composition surface.

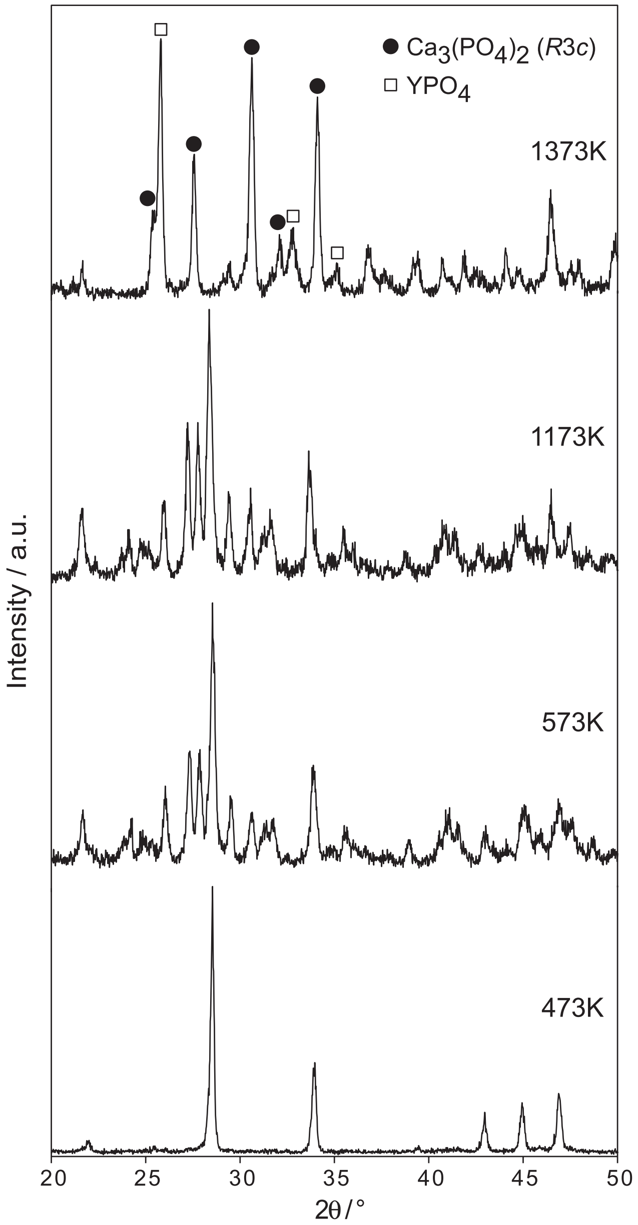

Fig. 9. Change in XRPD pattern induced by the martensitic transformation and decomposition reaction of $Ca_3Y(PO_4)_3 \rightarrow Ca_3(PO_4)_2 + YPO_4$ during heating to 1373 K.

we schematically prepared the time–temperature-transformation (TTT) diagram of the two reactions. The upper two C-shaped curves in Fig. 10 give, respectively, the relation between time and temperature for the start (left) and the finish (right) of the decomposition reaction. The upper broken line in the figure gives the lower limit of the stable temperature range of eulytite (T_e). The T_e temperature was determined to be 1488 K in a previous study [2]. With the martensitic transformation, the progress was inhibited by rapid cooling, and hence the transformation would be isothermal. Accordingly, the fraction transformed was displayed by the two C-shaped curves on the lower part of the diagram (Fig. 10).

The cooling curves in Fig. 10 are for the linear cooling rates between 200 K/s and 1.7 K/min from T_e. By superposing these curves on the TTT diagram, we can predict the phase constitution at ambient temperature. The cooling curve for a rate higher than 200 K/s does not cross any starting curves and hence the eulytite-type $Ca_3Y(PO_4)_3$ is quenched at ambient temperature. For cooling rates of 7 and 1 K/s, the martensitic transformation occurs at ~1000 K and the inverted eulytite will be preserved at ambient temperature. At cooling rates 0.7 K/s and 20 K/min, the decomposition reaction will start, but the process will not have been completed. For a cooling rate lower than 5 K/min, it is expected that the eulytite-type $Ca_3Y(PO_4)_3$ entirely decomposes into β-$Ca_3(PO_4)_2$ and YPO_4.

4. Conclusion

We investigated the crystal structures and phase transformations of calcium yttrium orthophosphate. The high-symmetry phase (space group $I\bar{4}3d$) was isostructural with eulytite. The structure was successfully expressed by a split-atom model, the oxygen atoms in which were distributed over two partially occupied sites. Below the stable temperature range of eulytite, the martensitic transformation occurred. The inverted eulytite (space group $P1$) showed pseudo-merohedral twinning, the adjacent twin domains of which were related by

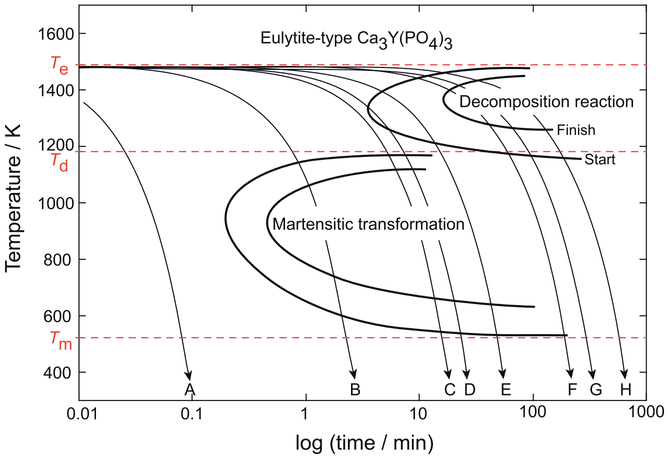

Fig. 10. Schematic TTT diagram illustrating the relative positions of the C-shaped curves for isothermal martensitic transformation and decomposition reaction. The temperature T_e (= 1488 K) refers to the equilibrium lower limit of the stable temperature range of eulytite [2]. The temperatures T_d (= 1182 K) and T_m (= 523 K) determined by DTA. The linear cooling curves from T_e in logarithmic scale are for (A) 200 K/s, (B) 7 K/s, (C) 1 K/s, (D) 0.7 K/s, (E) 20 K/min, (F) 5 K/min, (G) 3.3 K/min and (H) 1.7 K/min.

the pseudo-symmetry mirror planes parallel to $\{10\bar{1}\}$ and separated by the composition surface parallel to $\{10\bar{1}\}$. When the eulytite was cooled relatively slowly from the stable temperature range, the decomposition reaction of $Ca_3Y(PO_4)_3 \rightarrow \beta\text{-}Ca_3(PO_4)_2 + YPO_4$ occurred.

References

[1] W. Szuszkiewicz, J. Therm. Anal. 43 (1995) 187–192.
[2] W. Szuszkiewicz, T. Znamierowska, J. Solid State Chem. 88 (1990) 406–410.
[3] D.J. Segal, R.P. Santoro, R.E. Newnham, Z. Kristallogr. 123 (1966) 73–76.
[4] P. Fischer, F. Waldner, Solid State Commun. 44 (1982) 657–661.
[5] J. Barbier, J.E. Greed, T. Asaro, G.J. McCarthy, Eur. J. Solid State Inorg. Chem. 27 (1990) 855–867.
[6] El H. Arbib, B. Elouadi, J.P. Chaminade, J. Darriet, Mater. Res. Bull. 35 (2000) 761–773.
[7] J. Barbier, J. Solid State Chem. 101 (1992) 249–256.
[8] C.W. Wayman, in: R.W. Cahn, P.H. Haasen (Eds.), Physical Metallurgy, Elsevier Science Publishers BV, New York, 1983, pp. 1031–1074.
[9] G.L. Nord Jr., in: P.R. Buseck (Ed.), Minerals and Reactions at the Atomic Scale: Transmission Electron Microscopy, BookCrafters, Michigan, 1992, pp. 455–508.
[10] F. Izumi, R.A. Dilanian, in: Recent Research Developments in Physics, Part II, vol. 3, Transworld Research Network, Trivandrum, India, 2002, pp. 699–726.
[11] C. Dong, J. Appl. Crystallogr. 32 (1999) 838.
[12] P.E. Werner, L. Eriksson, M. Westdahl, J. Appl. Crystallogr. 18 (1985) 367–370.
[13] P.M. de Wolff, J. Appl. Crystallogr. 1 (1968) 108–113.
[14] G.S. Smith, R.L. Snyder, J. Appl. Crystallogr. 12 (1979) 60–65.
[15] F. Izumi, T. Ikeda, Mater. Sci. Forum 321–324 (2000) 198–203.
[16] H. Toraya, J. Appl. Crystallogr. 23 (1990) 485–491.
[17] R.A. Young, in: R.A. Young (Ed.), The Rietveld Method, Oxford University Press, Oxford, UK, 1993, pp. 1–38.
[18] R.D. Shannon, Acta Crystallogr. A 32 (1976) 751–767.
[19] G.S. Pawley, J. Appl. Crystallogr. 14 (1981) 357–361.
[20] H. Toraya, J. Appl. Crystallogr. 19 (1986) 440–447.